Analytical and Experimental Performance of a Dual-Mode Traveling-Wave Tube and Multistage Depressed Collector

Peter Ramins,
Dale A. Force, and
Henry G. Kosmahl

NASA

Analytical and Experimental Performance of a Dual-Mode Traveling-Wave Tube and Multistage Depressed Collector

Peter Ramins,
Dale A. Force, and
Henry G. Kosmahl

Lewis Research Center
Cleveland, Ohio

Summary

Experimental verification is presented for a computational design procedure for traveling-wave tubes (TWT's) equipped with short, permanent-magnet refocusers and multistage depressed collectors (MDC's). As in previous work of this kind, multidimensional computer programs are used to describe the interaction of the electron beam with the electric and magnetic fields of the TWT, refocuser, and MDC. The electron beam is modeled as a series of 32 disks of charge per radiofrequency (RF) cycle, and the trajectories of these representative charges are computed from the RF input of the TWT to their points of impact on the electrodes of the MDC. The trajectory computation in the refocuser is treated as a time-dependent problem, and includes modeling of the dissipation of axial space charge (debunching). A semiquantitative technique is used to analyze the reduction in collector efficiency due to backstreaming secondary-electron-emission current from the collector electrodes.

The procedure was used to design a short, permanent-magnet refocuser and a small-sized MDC for a 4.8- to 9.6-GHz, medium-power, dual-mode TWT. The refocuser deviated from the traditional concept of controlled beam expansion and improved laminarity, as evidenced by a reduction in the standard deviation of injection angles at the MDC entrance. The magnetic field profile in the refocuser was considered to be an independent variable to maximize the power recovered in the collector (and, therefore, the collector and overall efficiencies) without regard to beam expansion and injection angles, as such. Isotropic graphite electrodes were used in the MDC to reduce secondary-electron-emission losses.

In general, good agreement was obtained between the computed and measured results. The computed and measured collector efficiencies were comparable to those obtained previously with beam expansion and optimized refocusing in conjunction with the same basic model TWT and small-sized MDC. Reduction in TWT overall and collector efficiencies due to backstreaming secondary-emission current in the MDC is illustrated and computed, and the need to provide built-in suppression of secondaries by proper MDC design is discussed.

Introduction

In reference 1, a computational procedure for the design of TWT's equipped with short, permanent-magnet, spent-beam refocusing systems and MDC's was presented. The electron beam in the refocuser was analyzed as a time-dependent, or dynamic, beam by using the Lewis Research Center's large-signal, helical TWT computer program. This made possible the design of short, permanent-magnet "dynamic refocusing" systems, situated next to the RF output of the TWT, which provide simultaneous beam debunching and reconditioning. The MDC analysis included a semiquantitative treatment of secondary-electron-emission losses in MDC's. In general, very good agreement was found between the computed and measured performance of a 300-W, 8- to 18-GHz TWT. The work was conducted at the NASA Lewis Research Center under a program (conducted, in part, jointly with the U.S. Air Force) to improve the performance of TWT's, and to reduce the risk, time, and cost of tube acquisition.

In a continuation of this program, the computational procedure was used to design a short, permanent-magnet refocuser and small-sized MDC for an existing 4.8- to 9.6-GHz, medium-power, dual-mode TWT (Teledyne MEC model MTH-7000). The refocuser and MDC were fabricated, and an experimental program was conducted to evaluate the TWT-MDC performance under a variety of operating conditions. Isotropic graphite electrodes were used in the MDC to reduce secondary-electron-emission losses.

In the following report, the computer models, the analytical and experimental procedures, and the tube characteristics are briefly described; the results of the TWT, refocuser, and MDC analyses are discussed; and comparisons of analytical and experimental results are presented.

Symbols

E disk energy, keV

I_{en} net current to collector electrode n, A

I_G total body current, including backstreaming from collector, A

I_0 beam current, A

P_{body} body power, sum of RF circuit losses and intercepted-beam power in forward direction, W

P_{col} collector power, $V_0 I_0 - P_{RF} - P_{body}$, W

P_{rec} recovered power, $\displaystyle\sum_{n=1}^{4} V_{en} I_{en}$, W

P_{RF} total RF output power, W

P' prime power, $V_0 I_G + \displaystyle\sum_{n=1}^{4} (V_0 - V_{en}) I_{en}$, W

r disk-edge radius, m

V_{en} voltage on collector electrode n with respect to ground, V

V_0 cathode potential with respect to ground, V

η_c TWT circuit efficiency, $P_{RF}/(P_{RF} + \text{circuit losses})$, percent

η_{col} collector efficiency, P_{rec}/P_{col}, percent

η_e electronic efficiency, η_{RF}/η_c

η_{ov} TWT overall efficiency, P_{RF}/P', percent

η_{RF} RF efficiency of TWT, $P_{RF}/V_0 I_0$, percent

θ disk-edge angle, deg

Analytical Models and Computer Programs

Overall System

For the purpose of analysis, the system was divided into three parts: (1) the TWT between the RF input and output, (2) the "dynamic refocusing" region, and (3) the MDC. The first two parts of the calculation were performed by using the NASA Lewis Research Center's large-signal, multidimensional, helical TWT program. In this program, the electron beam is modeled as a number of deformable disks of charge per RF cycle, which interact with the static and time-varying (RF) fields in the TWT. The trajectories of the disks are tracked through the tube and the dynamic refocusing system. In part (3) of the calculation it is assumed that all RF current has dissipated, and each disk is replaced by a continuous (dc) ray of current at the center of charge of the disk. The trajectories of these current rays were computed by using the Herrmannsfeldt Electron Trajectory Program (ref. 2).

Traveling-Wave Tube

In the TWT, disk trajectories in the presence of RF circuit forces, space-charge forces, and magnetic focusing fields are computed from the RF input of the TWT to the RF output. At the RF output, the computer program lists the following:
  (1) RF output power
  (2) RF circuit losses
  (3) Sever and attenuator losses
  (4) Intercepted current and power
  (5) Radial coordinates of the disk edges
  (6) Three components of velocity ($\dot{r}$, $\dot{\varphi}$, $\dot{z}$) of each disk
  (7) Relative phase of each disk
The trajectory program does not include effects of thermal velocities on the radial and azimuthal motion. According to Herrmann's optical theory of thermal effects in electron beams,

these effects should be relatively small for a tube with a medium or higher perveance.

At the RF output, the electron beam is tightly bunched, causing strong space-charge forces to exist between disks.

Dynamic Refocusing System

The description of the spent beam at the RF coupler of the TWT provides the input data for the refocusing system calculations. The refocusing system is situated just downstream of the RF output coupler, and simultaneous beam debunching and reconditioning is accomplished in this section. The beam characteristics at the end of the refocusing section define the input conditions to the MDC.

A modification in the method of utilization of the TWT program (ref. 1), adopted after the completion of the computations described here, permits the computation of the electron beam flow in a region where the tunnel diameter changes discontinuously. This permits the analysis of a wide variety of possible refocuser configurations. The effect on the spent beam of debunching and reconditioning in the refocuser is treated simultaneously.

Multistage Depressed Collector

The computation of the trajectories in the MDC treats the disks as continuous rays of current; that is, complete debunching (or dissipation of RF current in the beam) is assumed. Each current ray is located at the centroid of charge of its corresponding disk and has the vector velocity of the disk centroid. The trajectory calculation is continued until the current rays strike the MDC electrodes. The effect of secondary electron emission from electrode surfaces is analyzed by injecting one or more representative subcharges at the points of impact of the primary current rays and by tracking these secondary charge trajectories to their final termination within the MDC or TWT. The effects of further secondary electron emission due to these secondaries are neglected. Based on the final location of the primary and secondary charges, a calculation is made of the collected current, recovered power, and dissipated power at each of the collector electrodes and, if backstreaming occurs, at the TWT itself. These results, when coupled with the outputs of the TWT computer program, provide a detailed picture of the current and power flow with the TWT-MDC system.

Characteristics of Traveling-Wave Tube and Multistage Depressed Collector

A modified version of Teledyne MEC TWT model MTH-5065 was used in this program. The MTH-5065 has a helical, slow-wave circuit and periodic permanent magnet (PPM) focusing. Two permanent magnets past the RF output coupler, in a continuation of the PPM stack, constituted the
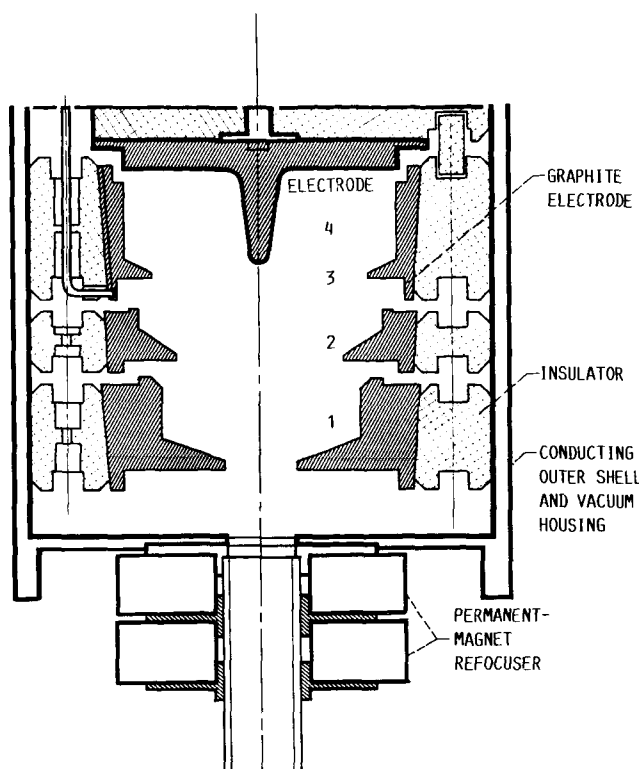
Figure 1.—Cross section of four-stage, brazed-graphite, depressed collector and permanent-magnet refocusing system.

refocusing system of 1.25 magnetic periods. The general tube operating characteristics were as follows:

Frequency, GHz .... 4.8 to 9.6
Beam voltage, kV 9.75
Beam current, A
  High mode 0.48
  Low mode 0.38
Nominal output power, W
  High mode 750
  Low mode 500
Duty cycle, percent
  High mode 50
  Low mode 100

A NASA Lewis designed and fabricated MDC (ref. 3), shown in figure 1, utilizing four separate brazed-graphite electrodes was used in these tests. The MDC was designed to be conduction cooled to the existing TWT baseplate. The MDC was delivered to Teledyne MEC for integration with the TWT, bakeout, and RF focusing/processing.

Analytical and Experimental Procedure

A computational procedure using 32 disks per RF cycle to model the beam was used to design a refocusing system and a four-stage depressed collector for the TWT, with small size,

simplicity, and ease of fabrication in mind. The MDC design was largely optimized for saturated operation of the TWT in the low, continuous wave (CW), mode.

The TWT used in this program (MTH-5065) was almost identical to Teledyne MEC model MTZ-7000, which had been analyzed (and tested) previously in conjunction with a relatively long, variable refocusing system and a number of MDC's (ref. 4). Consequently, because the differences in the RF circuits of these TWT's were believed to be inconsequential, the spent-beam models generated for MTZ-7000 were used to design the refocuser and MDC. These beam models corresponded to saturated operation in both the high and low modes at the frequency (8.4 GHz) yielding the highest TWT RF efficiency.

Since the TWT analysis already modeled two full-strength permanent magnets past the RF output (in a continuation of the PPM stack of 1¼ magnetic periods), it was decided to attempt to design an efficient MDC for this (existing) refocuser magnetic field profile, and to resort to separate refocusing system optimization (beam expansion with weaker magnets) only if high collector efficiencies could not be obtained. This approach was successful, and MDC efficiencies comparable to those obtained previously with optimized beam expansion in conjunction with MTZ-7000 and a small-sized collector (ref. 4) were produced. Consequently, the refocuser optimization was not necessary.

A semiquantitative technique was used to investigate the effect of any backstreaming, low-energy, secondary-electron-emission current from the collector electrode surfaces, and the attendant reduction in collector efficiency. Secondary-electron-emission current in the amount $0.6I_i$, where I_i is the incident current, was injected at the points of impact of the primary charges on the MDC electrodes. This value of total secondary-electron-emission yield (0.6) was based on reference 5, and represents an average value for the range of primary energies and angles in incidence under consideration. The initial conditions for this secondary-electron-emission current corresponded to injection back along the angle of incidence of the primary charges at an energy of 10 eV per electron. Collector efficiencies were computed with and without this representative secondary electron emission.

A better simulation (other energies and angles of injection) is readily possible; however, detailed measurements of secondary-electron-emission characteristics (the angular and energy distributions) of modern MDC electrode materials (e.g., isotropic graphite) are not generally available. Furthermore, more complex simulations involve additional computer time and may not be cost effective.

A TWT (model MTH-5065) equipped with the graphite-electrode MDC was fabricated and experimentally evaluated at a number of distinct TWT-MDC operating conditions, in both three-stage and four-stage configurations. (The number of stages is defined as the number of distinct voltages, other than ground, required to operate the MDC.) In the three-stage simulation of the four-electrode collector (which was not

analyzed prior to testing of the TWT-MDC), electrodes 1 and 2 were electrically connected.

The selected MDC operating conditions for saturated operation of the TWT at 8.4 GHz in both the high and low modes were the following:

(1) analytical design voltages of the four-stage collector
(2) experimentally optimized voltages of the four-stage collector
(3) experimentally optimized voltages of the three-stage collector

The MDC analyses were then performed for operating conditions (2) and (3). Because an unusual sensitivity of collector efficiency to operating voltages was observed for operating condition (3) (discussed in the section **Multistage Depressed Collector Analysis Results and Comparison With Measurements**), the three-stage collector performance was both measured and analyzed for slightly reduced (from experimentally optimized) voltages as well. The following sections give the results of the TWT, refocusing system, and MDC analysis and present a comparison of the analytical and experimental TWT and three- and four-stage collector performance for the operating conditions described in the preceding paragraph.

However, because the TWT was not operated first with an undepressed collector (which produces only negligible backstreaming power) and the TWT and the MDC electrodes were conduction cooled to a single baseplate, it was not possible to present the detailed picture of power flow in the experimental TWT and MDC given in reference 4. Furthermore, the computation of collector efficiency made the assumption that the experimental TWT exhibited the same body power characteristics as MTZ-7000, serial number 103 (ref. 4).

Traveling-Wave-Tube Analysis Results and Comparison With Measurements

The computed and measured RF performance is shown in table I. Since the tube operating parameters (table II) for the analytical design case and the experimental TWT (MTH-5065, serial number 001, called TWT 001 hereinafter) differ somewhat, the results in this and in subsequent sections of this report are shown as percentages of V_0, I_0, and $V_0 I_0$, where V_0 is cathode potential with respect to ground and I_0 is beam current. For convenience, the experimental data were obtained at duty cycles of 50 and 25 percent for the low and high modes, respectively. The experimental circuit efficiencies shown in table I are the measured values for TWT model MTZ-7000, and the electronic efficiencies of TWT 001 are based on these estimates.

As discussed in the preceding section, the TWT analysis was performed by using the parameters of MTZ-7000, and very good agreement had been obtained between computed and measured values for MTZ-7000 (ref. 4). The agreement with the measured performance of TWT 001 is not nearly as

good. In the low mode TWT 001, which has a slightly longer RF circuit output section, produced considerably more output power P_{RF}. In the high mode, however, where the value of beam current (475 mA) was selected to match the perveance of the analytical case, the electronic efficiency η_e was only slightly higher than for the low mode (table I). The RF and electronic efficiencies peaked at 17.2 and 20.6 percent, respectively, at a much lower value of beam current (417 mA). At this level of beam current the measured electronic efficiency closely matches the computed one. The gradual but steady decline in these efficiencies for increasing values of beam current might be explained if the observed rapid, simultaneous increase in total body current I_G was largely due to true beam interception somewhat before the RF output. This behavior was not exhibited by the model MTZ-7000 TWT.

The spent-beam energy distributions for the high and low modes at saturation, after axial debunching in the refocuser, are shown in figure 2. The range of electron energies is larger for the high mode because of the larger beam perveance and electronic efficiency (ref. 6). The effect of axial debunching is illustrated in figure 3. The spent-beam energy distribution is considerably altered, especially for the high mode. As shown in the next section, the resulting energy exchange between the disks is as high as several keV.

Refocusing System Analysis Results

The very simple refocusing system consisting of two full-strength magnets past the RF output coupler, in a continuation of the PPM stack, was found to be acceptable. A single magnet had to be added to the existing PPM stack of the production model TWT. The beam debunching in the refocuser has already been discussed in the section **Analytical Models and Computer Programs**. The charge trajectories through the refocusing region are shown in figure 4. The tunnel wall in figure 4 corresponds to a continuation of the helix of the TWT.
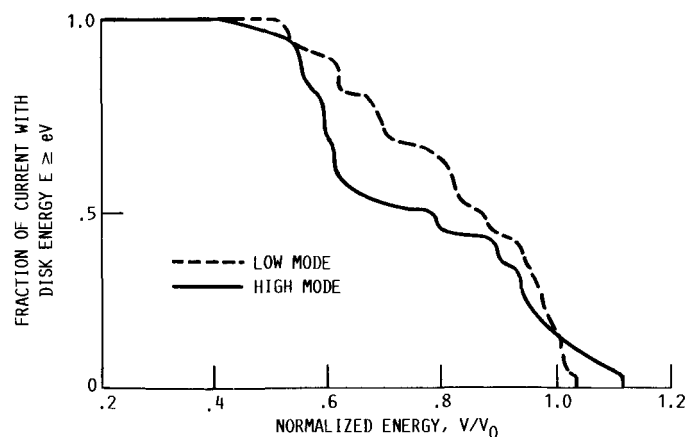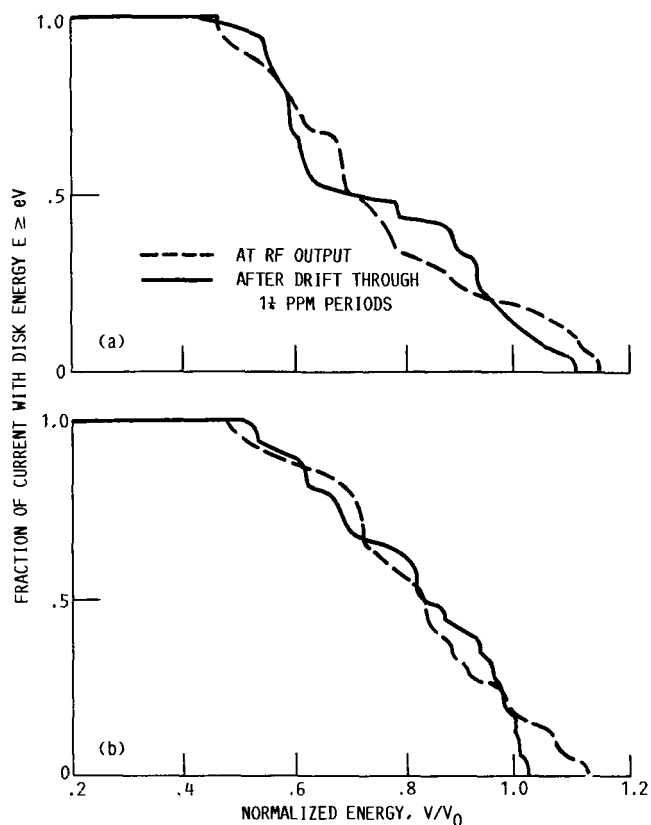

Figure 2.—Computed spent-beam energy distributions of high and low modes at saturation after debunching. For high mode, electronic efficiency η_e, 0.205; perveance, 0.5×10^{-6} A/V$^{3/2}$. For low mode, η_e, 0.15; perveance, 0.4×10^{-6} A/V$^{3/2}$.

(a) High mode. TWT electronic efficiency η_e, 0.205; perveance, 0.5×10^{-6} $A/V^{3/2}$.

(b) Low mode. TWT electronic efficiency η_e, 0.15; perveance, 0.4×10^{-6} $A/V^{3/2}$.

Figure 3.—Computed spent-beam energy distribution before and after debunching for TWT operation at saturation.

In the experimental TWT the beam moves through a tunnel of somewhat larger radius. Any effect on the beam due to this smaller drift tunnel diameter was neglected. The 0.3 percent beam interception on the "nonexistent" tunnel wall was also neglected.

The disk energies, angles, and radii at the input and the output of the refocuser are shown in tables III to V. A slight beam expansion takes place in the low mode. For the high mode, however, the beam is slightly radially compressed. The average energy of the disks is virtually unchanged, although there are very large exchanges of energy (up to several keV) between disks. The total range of energies (and the standard deviation) has been reduced slightly. The number of disks with negative angles has been increased as well as the standard deviation of the angles. The average angle of the disk edge is negative for both modes, at the output of the refocuser. According to traditional criteria for judging the quality of spent-beam reconditioners (refs. 7 to 10), this does not appear to be a good spent-beam refocuser. The trajectories in the refocuser evidence considerable disorder (nonlaminarity) compared to the cases of optimized refocusing with beam expansion for the same TWT (e.g., fig. 4 of ref. 4). However, as discussed in the next section, it was possible to design a highly efficient collector for this beam. Consequently, this refocusing system was selected for its simplicity and ease of fabrication (a single magnet had to be added to the PPM stack of the production version of TWT model MTH–5065).

At the outset of this program, it was envisioned that the refocusing system profile would be optimized by individually trimming the strength of the two refocusing-system magnets, within the range of ±10 percent, and by shunting the magnets to optimize the TWT overall efficiency. The strength of the
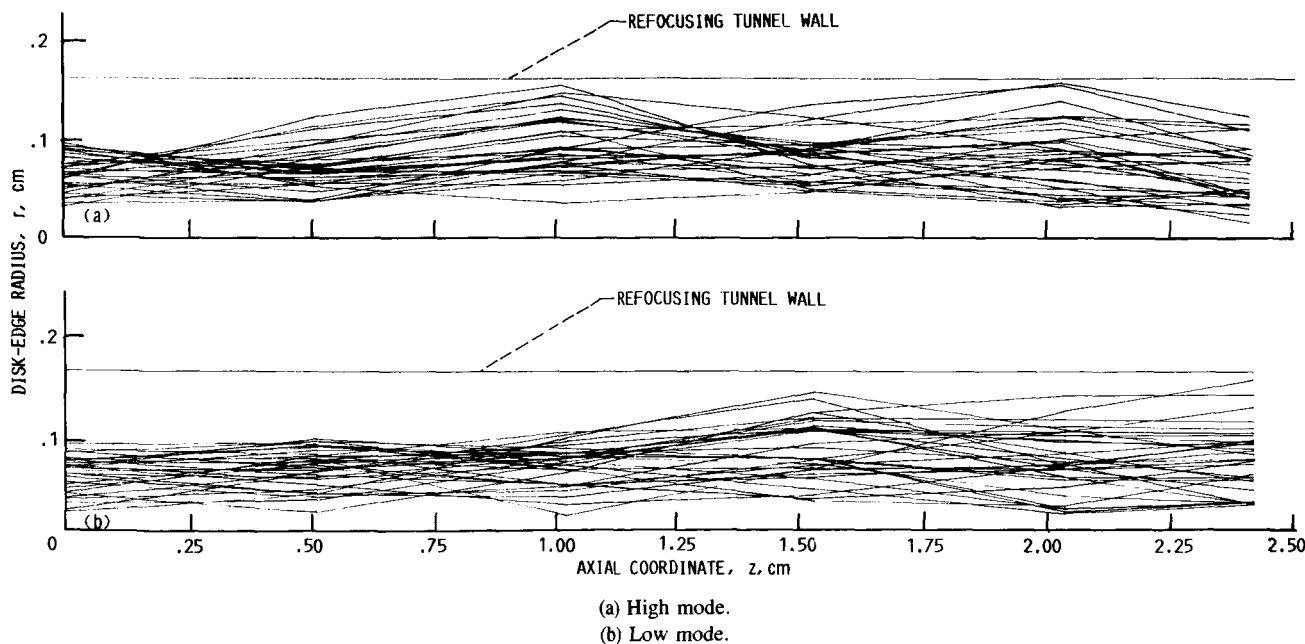

(a) High mode.

(b) Low mode.

Figure 4.—Charge trajectories in refocusing section for TWT operation at saturation.

final magnet, in particular, represents an independent variable that can be used to maximize the recovered power P_{rec} without affecting the RF output power. However, because of the favorable results obtained with the nominal refocuser, such optimization was not performed.

Multistage Depressed Collector Analysis Results and Comparison With Measurements

Traveling-Wave Tube and Four-Stage Collector

The four-stage, axisymmetric, MDC geometry, the applied potentials, the equipotential lines, and the trajectories of primary- and representative secondary-electron-emission charges are shown in figures 5 and 6 for the low and high modes, respectively, for the analytical design case voltages. The corresponding results, for the case of experimentally optimized collector voltages, are shown in figures 7 and 8. The detailed analytical and experimental TWT-MDC performances are compared in detail in tables VI to IX. The computed and measured RF, overall, and collector efficiencies are summarized in table X.

Figures 5 to 8 show that, for the most part, the low-energy (10 ev) secondary electron emission is effectively suppressed by the local electron field. However, this is not the case for a substantial area of electrode 3, as can be seen from the backstreaming secondary current in figure 5. For the analytically determined voltages, the entire top surface (top of figure) of electrode 3 between the inner aperture and the corner (beginning of the vertical section) provides inadequate suppression of secondary electrons. Over part of the electrode area near the inner aperture, shown by dashed lines inside the electrode boundry, the local electric field actually accelerates secondary electrons away from the electrode. Over the remainder of the top surface of electrode 3 out to the corner (vertical section), the local electron field is too weak to suppress all but the lowest energy (a few eV) secondaries. For the case of experimentally optimized voltages, the suppression is slightly better.

This design deficiency can largely be avoided by a modified collector geometry. The current design was implemented because only a small amount of current struck this area in the low mode, and none in the high mode. However, in the experimental MDC, it can be safely assumed that all top surfaces of the electrodes receive some current. Better modeling of the beam, by using a number of current rays in the MDC for each disk in the TWT-refocuser (instead of the single current ray at the center of charge of the disk), would confirm this.

The computed degradations in the TWT overall and MDC efficiencies due to backstreaming secondary electron emission in the collector are shown in tables XI and XII for the low and high modes, respectively. These computed degradations,

Figure 5.—Trajectories of primary- and secondary-electron-emission charges in four-stage, 2.4-cm-diameter collector operating at analytically determined voltages. TWT operating at saturation in low mode. Dashed lines indicate surfaces where electric field accelerates secondary electrons away from electrode.

which do not consider the effects of elastically and inelastically reflected primaries, are substantial. This is particularly true for the low mode because a larger amount of primary current is incident on electrode areas which do not provide adequate suppression of secondaries.

For the high mode, experimental TWT-MDC performance (tables VII and IX) was obtained for beam currents of 0.417 A and 0.475 A because of the peculiar behavior exhibited by the experimental TWT, as discussed in the section **Traveling-Wave-Tube Analysis Results and Comparison With**
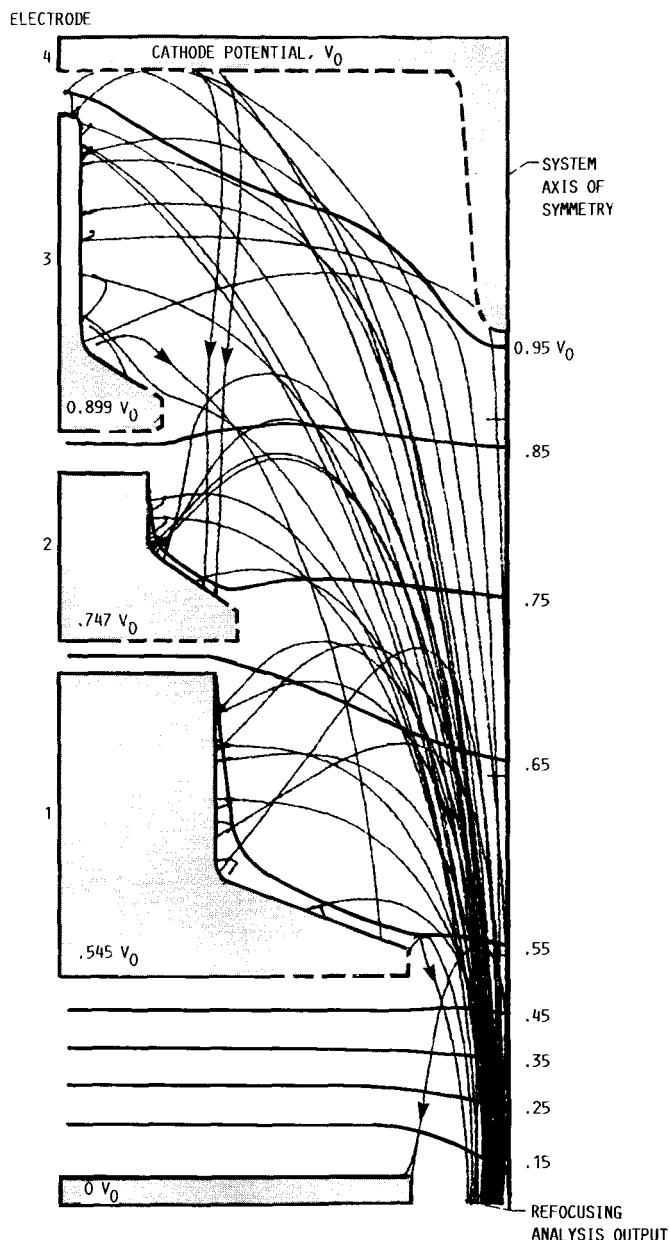
6

Figure 6.—Trajectories of primary- and secondary-electron-emission charges in four-stage, 2.4-cm-diameter collector operating at analytically determined voltages. TWT operating at saturation in high mode.

Figure 7.—Trajectories of primary- and secondary-electron-emission charges in four-stage, 2.4-cm-diameter collector operating at experimentally optimized voltages. TWT operating at saturation in low mode.

Measurements. At a beam current of 0.417 A, the RF efficiency (17.2 percent) more nearly matches the computed case, and the characteristics of total body current I_G as a function of beam current more nearly match those of TWT MTZ–7000 (on which body power estimates are based). If the significantly larger body current I_G of TWT 001 at $I_0 = 0.475$ A (as compared to MTZ–7000) is primarily due to large beam interception, then the collector efficiencies in the high mode (at $I_0 = 0.475$ A) are somewhat underestimated, since they are based on the measured body power of MTZ–7000.

The experimental TWT-MDC performance was optimized for the low mode so that the maximum CW prime power could be minimized. It is also nearly optimum for the high mode at a beam current of 0.417 A, but less so at 0.475 A.

The computed and measured collector efficiencies show very good agreement, in particular, for the low mode and for a beam current of 0.417 A in the high mode. The measured collector efficiencies at the analytical voltages are slightly lower than predicted, but they very nearly matched the predictions when the voltages were experimentally optimized. Experimental optimization of the refocusing system profile was not required. The agreement between computed and measured overall efficiencies is not as good because of differences between the computed and measured TWT RF efficiencies, and because

7

Figure 8.—Trajectories of primary- and secondary-electron-emission charges in four-stage, 2.4-cm-diameter collector operating at experimentally optimized voltages. TWT operating at saturation in high mode.
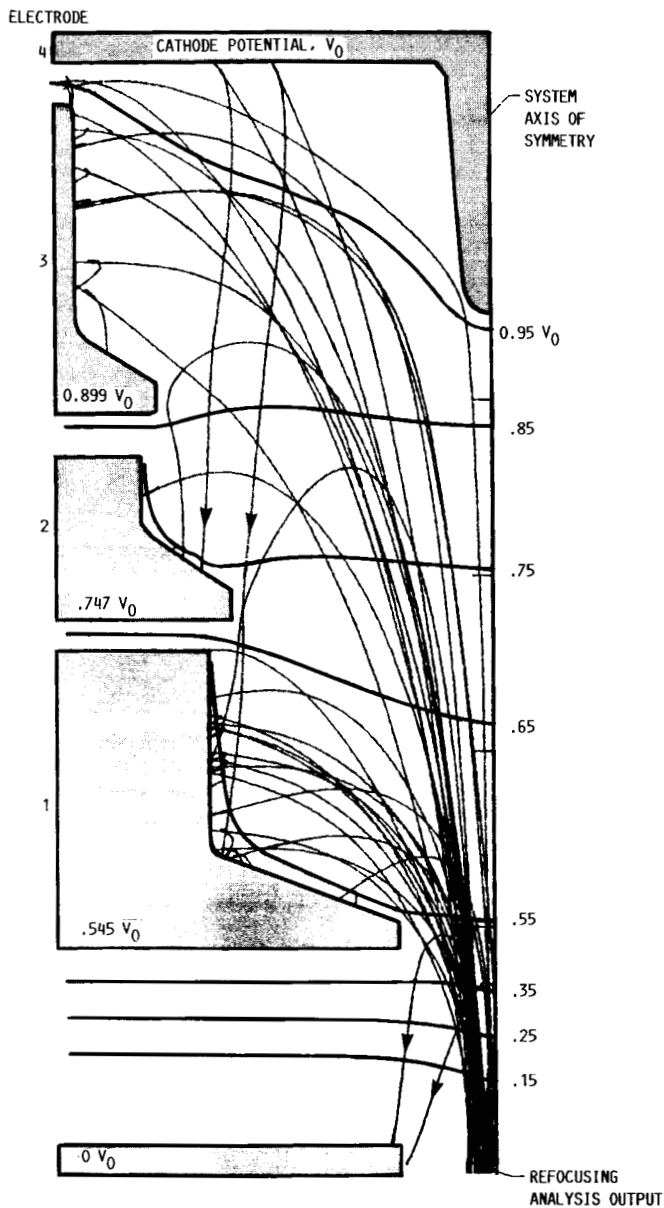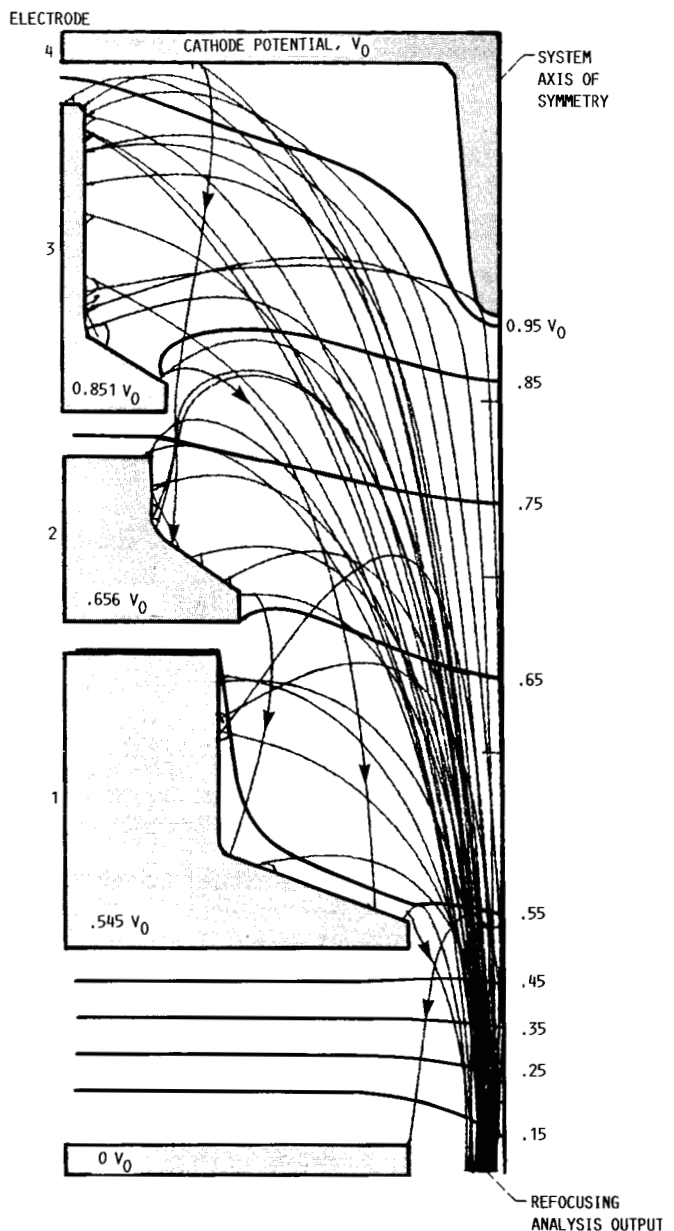

Figure 9.—Trajectories of primary- and secondary-electron-emission charges in three-stage, 2.4-cm-diameter collector operating at experimentally optimized voltages. TWT operating at saturation in low mode.

of zero beam interception for the computed case. For the case of the high mode, the computed and measured current distributions in the collector show reasonably good agreement.

Both the predicted and measured collector efficiencies match very closely those obtained previously with beam expansion and optimized refocusing, and the four-stage, small-sized (2.4-cm-diam) collector designed for TWT model MTZ-7000 (refs. 4 and 11). This is somewhat surprising in view of the compressed, disordered (nonlaminar) beams at the output of the refocuser. However, when the beam size at the MDC input is much smaller than the collector size, disks with positive and negative angles become nearly indistinguishable to the col-

lector. Nor do the trajectories in figures 5 to 8 show uncontrolled expansion, which would lead to excessive radial velocities and attendant reductions in collector efficiency. The ratios of MDC radius to input beam-edge radius for the MDC's were the following:

	Collector radius/beam-edge radius[a]	
	High mode	Low mode
With expansion, MTZ-7000 (ref. 4)	2.9	3.0
Without expansion, MTH-5065	9.8	7.8

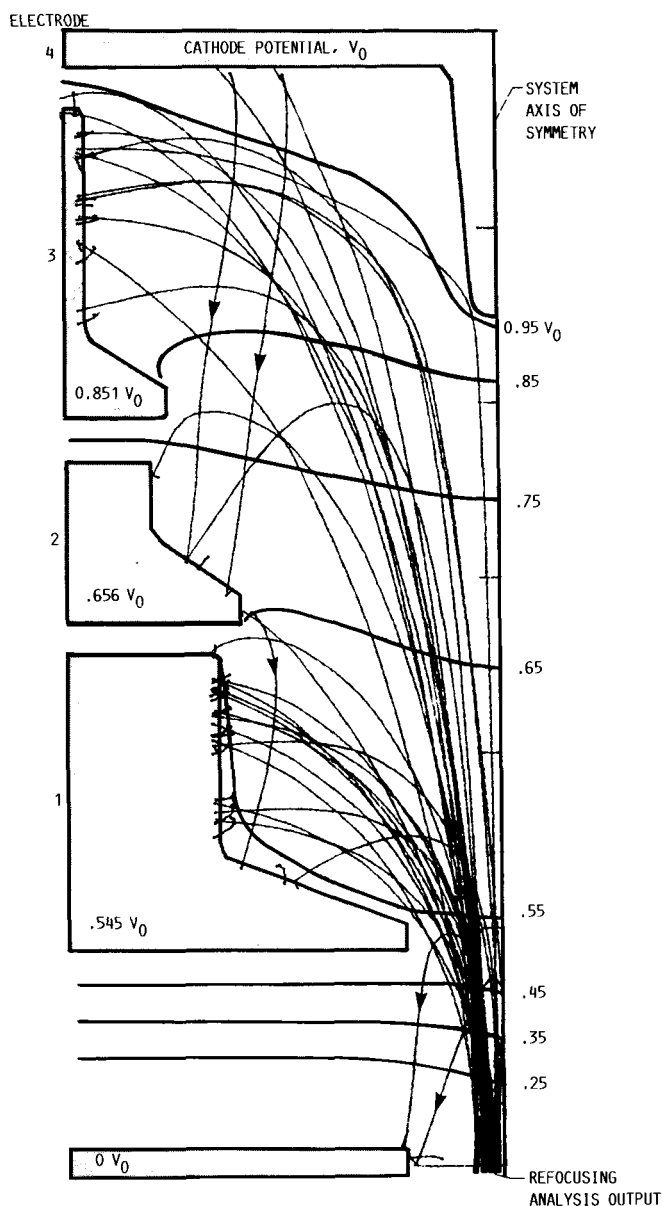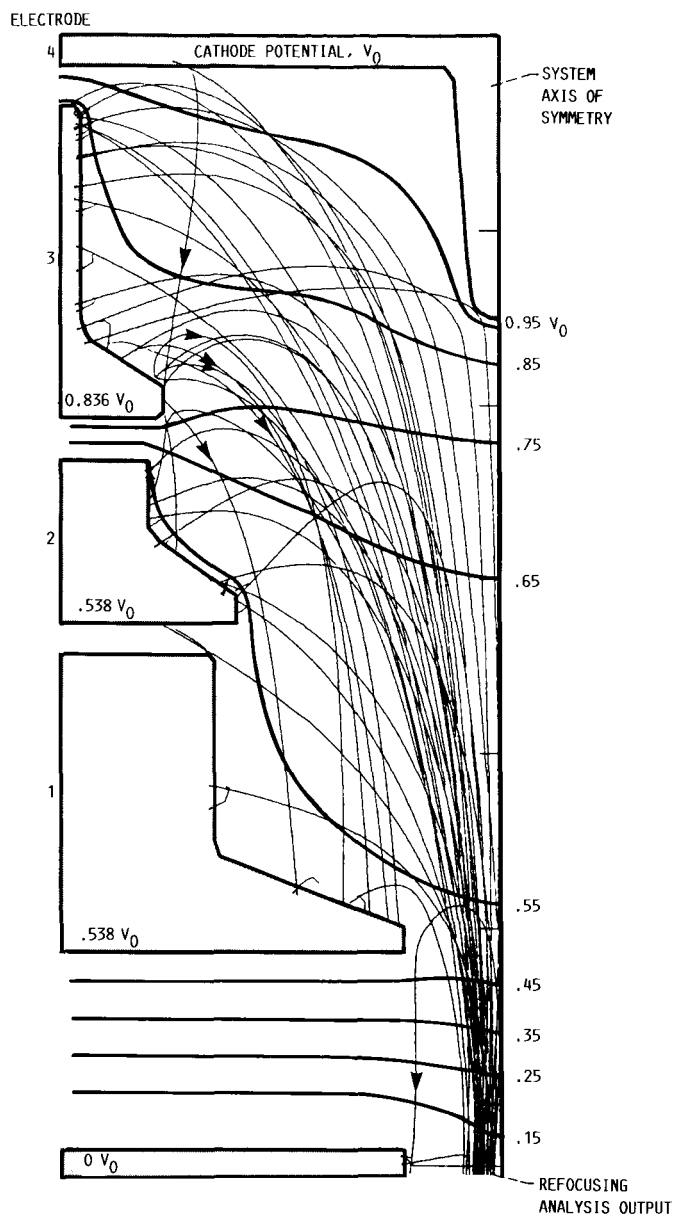[a]Largest computed disk-edge radius in beam at refouser output.

8

Figure 10.—Trajectories of primary- and secondary-electron-emission charges in three-stage, 2.4-cm-diameter collector operating at experimentally optimized voltages. TWT operating at saturation in high mode.

Figure 11.—Trajectories of primary- and secondary-electron-emission charges in three-stage, 2.4-cm-diameter collector operating at reduced voltages. TWT operating at saturation in low mode.

Traveling-Wave Tube and Three-Stage Collector

The three-stage, axisymmetric, MDC geometry, the applied potentials, the equipotential lines, and the trajectories of primary and secondary charges are shown in figures 9 and 10 for the low and high modes, respectively, for experimentally optimized voltages for the low mode. The corresponding results for the case of slightly reduced voltage applied to electrode 3 are shown in figures 11 and 12. The detailed analytical and experimental TWT-MDC performances are compared in tables XIII to XVI. The reduced-voltage cases were obtained because the computed results for the low mode and experimentally optimized voltages showed unusual sensitivity to the voltage applied to electrode 3. As can be seen

from figure 9, a substantial amount of current (more than 10 percent) impinges on the relatively small area where no suppression of secondary electron emission by the local electric field exists. Moreover, because of its particular energy and angle of injection at the entrance to the MDC, one of the charges is stopped before reaching the electrode and reflected inward and downward. This is also illustrated in figure 10. With a slight reduction in the voltage applied to electrode 3, the harmful backstreaming is considerably reduced, as shown in figure 11. The high mode, likewise, shows a high degree of sensitivity to the voltage applied to electrode 3 because of the reflection (and backstreaming) of a single charge to the TWT body, which reduces the collector efficiency by more
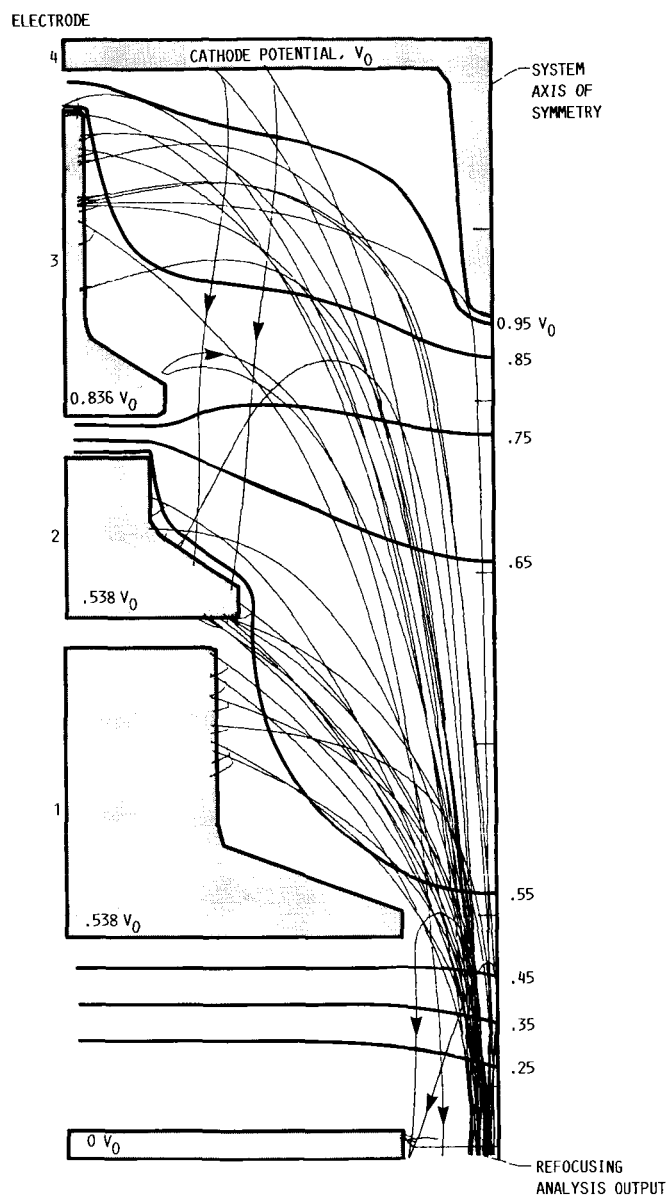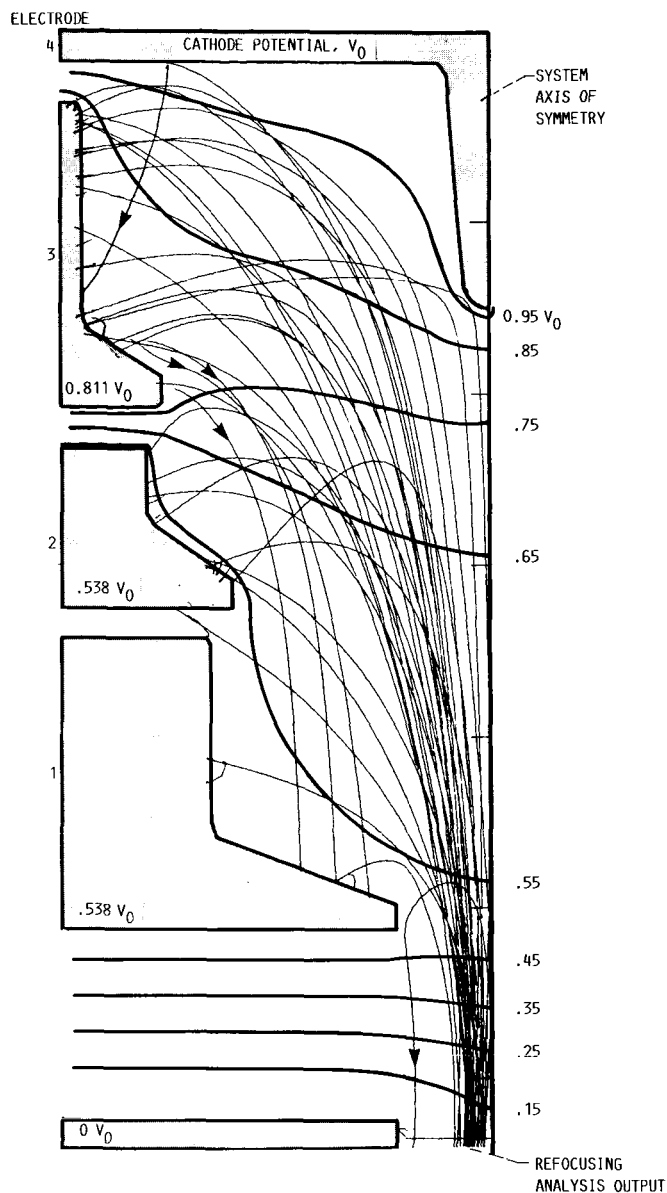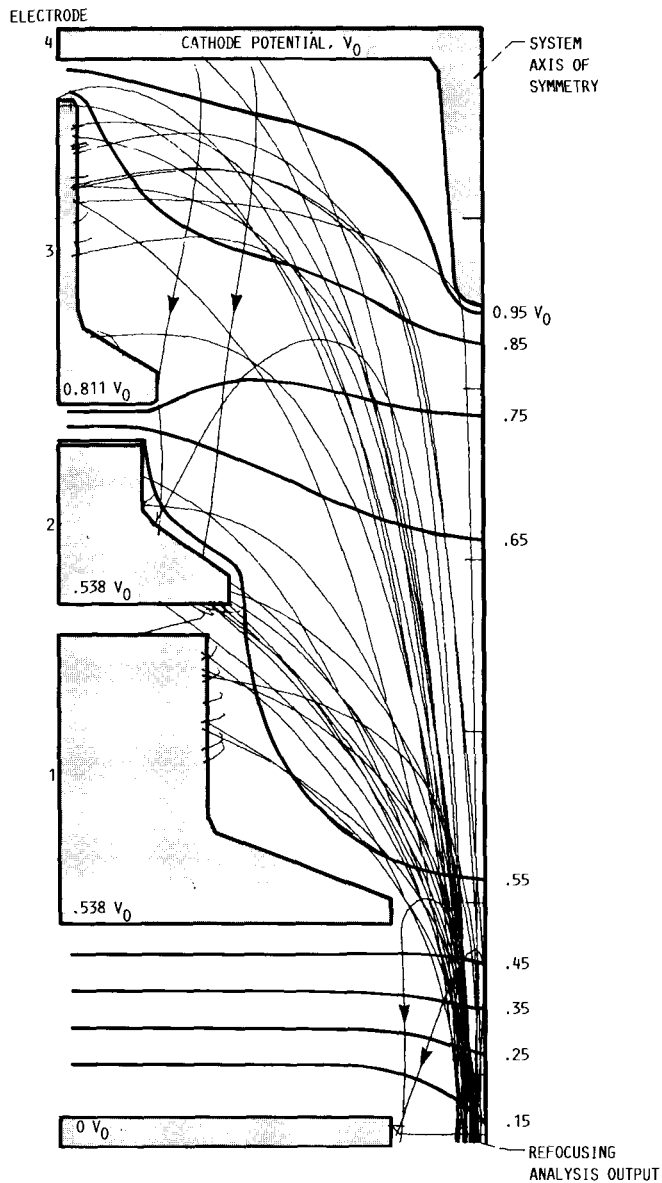
9

Figure 12.—Trajectories of primary- and secondary-electron-emission charges in three-stage, 2.4-cm-diameter collector operating at reduced voltages. TWT operating at saturation in high mode.

measured collector efficiencies show very good agreement. The high-mode cases show reasonably good agreement in the collector current distributions as well.

Concluding Remarks

The computer-aided design techniques described here produced a multistage depressed collector (MDC) that needed only adjustments of electrode voltages to achieve high efficiency. The planned experimental optimization of the strength of the permanent magnets of the refocusing system was not required.

The dynamic spent-beam analysis permits the designer to take into account the changes in the spent-beam energy distribution resulting from debunching, and this enables the design of short refocusers situated next to the RF output coupler of the traveling-wave tube (TWT) and more accurate MDC modeling. The refocusing system deviated from the traditional concept of controlled beam expansion and improved laminarily as evidenced by the reduction in the standard deviation of angles of injection into the MDC. The magnetic field profile in the refocuser was considered to be an independent variable to analytically and experimentally optimize the collector (and, therefore, overall efficiency) without regard to beam expansion and angles, as such.

In general, very good agreement was obtained between computed and measured collector efficiencies. The computed and measured collector efficiencies were comparable to those obtained previously with beam expansion and optimized refocusing, in conjunction with the same basic TWT model and small-size, four-stage collector. The inclusion of semi-quantitative, secondary-electron analysis provides greater accuracy in the determination of the loss of efficiency due to this effect and illustrates how it can be minimized. More elaborate models of secondary emission can certainly be implemented if warranted by the availability of secondary yield data and computational costs.

The results show that it is important to design the MDC such that the combination of geometry and applied potentials results in the suppression of low-energy, secondary-electron-emission current from all electrode surfaces (tops) which receive significant primary current. In the case of the most depressed electrode, the MDC should be designed to collect as much of the secondary-electron-emission current on the adjacent electrode as possible. This is particularly true for MDC's that utilize copper (or other materials with high secondary-electron-emission yield) for MDC electrodes, rather than the carbon electrodes used in the experimental MDC.

than 2 percent. Such sensitivity is largely due to the small number of charges (32) used to model the spent beam, and is not exhibited by the experimental TWT. The lack of secondary-electron-emission suppression from the top surfaces of the electrodes, and reflection of primary current by harmful lens effects in the collector can largely be avoided by suitably modifying the MDC geometry.

The computed and measured RF, overall, and collector efficiencies are summarized in table XVII. The computed degradations in the TWT overall efficiencies due to back-streaming secondary electron emission in the collector are shown in tables XVIII and XIX. In general, the computed and

Lewis Research Center
National Aeronautics and Space Administration
Cleveland, Ohio, May 11, 1987

References

1. Ramins, Peter; Kosmahl, Henry G.; Force, Dale A.; Palmer, Raymond W., and Dayton, James A., Jr.: Verification of Computer-Aided Designs of Traveling-Wave Tubes Utilizing Novel Dynamic Refocusers and Graphite Electrodes for the Multistage Depressed Collector. NASA TP-2524, 1985.

2. Herrmannsfeldt, W.B.: Electron Trajectory Program. SLAC-166, Stanford Linear Accelerator Center, Sept. 1973.

3. Ebihara, Ben T. and Ramins, Peter: Design, Fabrication, and Performance of Small, Graphite Electrode, Multistage Depressed Collectors with 200-W, CW, 8- to 18-GHz Traveling Wave Tubes. NASA TP-2693, 1987.

4. Dayton, J.A., Jr., et al.: Experimental Verification of a Computational Procedure for the Design of TWT-Refocuser-MDC Systems. IEEE Trans. Electron Devices, vol. 28, no. 12, Dec. 1981, pp. 1480-1489.

5. Curren, A.N.; and Jensen, K.A.: Secondary Electron Emission Characteristics of Ion-Textured Copper and High-Purity Isotropic Graphite Surfaces. NASA TP-2342, 1984.

6. Kosmahl, H.G.: How to Quickly Predict the Overall TWT and the Multistage Depressed Collector Efficiency. IEEE Trans. Electron Devices, vol. 27, no. 3, Mar. 1980, pp. 526-529.

7. Branch, G.M.; and Neugebauer, W.: Refocusing of the Spent Axisymmetric Beam in Klystron Tubes. NASA CR-121114, 1972.

8. Kosmahl, H.G.; and Ramins, P.: Small-Size 81- to 83.5-Percent Efficient 2- and 4-Stage Depressed Collectors for Octave-Bandwidth High-Performance TWT's. IEEE Trans. Electron, Devices, vol. 24, no. 1, Jan. 1977, pp. 36-44.

9. Stankiewicz, N.: Analysis of Spent Beam Refocusing to Achieve Optimum Collector Efficiency. IEEE Trans. Electron Devices, vol. 24, no. 1, Jan. 1977, pp. 32-36.

10. Krause, K.H.: A Dynamic Refocusing System for Linear Beam Microwave Tubes, Degree of Engineer Thesis, Stanford University, Stanford, CA, 1979.

11. Ramins, P.; and Fox, T.A.: Performance of Computer-Designed Small-Sized Four-Stage Depressed Collector for Operation of Dual-Mode Traveling Wave Tube. NASA TP-1832, 1981.

TABLE I.—COMPUTED AND MEASURED CIRCUIT, RF, AND ELECTRONIC
EFFICIENCIES OF TELEDYNE MEC DUAL-MODE TWT AT 8.4 GHz

TWT mode	Circuit efficiency,[a] η_c, percent		RF efficiency, η_{RF}, percent		Electronic efficiency, η_e, percent	
	Analytical	Experimental (MTZ-7000)	Analytical	Experimental[b] (TWT 001)	Analytical	Experimental[b] (TWT 001)
Low	88.6	86.1	13.5	16.7	15.2	19.5
High	86.1	83.5	17.6	16.4	20.5	19.6

[a]Computed by assuming the average energy of intercepted electrons is $e(V_0)(1 - \eta_e)$, where V_0 is cathode potential with respect to ground.
[b]Computed by using the measured circuit efficiency of MTZ-7000.

TABLE II.—ANALYTICAL AND EXPERIMENTAL
TWT OPERATING PARAMETERS

(a) Low mode

Parameter	Analytical design value	Experimental value for TWT
Cathode voltage, kV	9.9	9.75
Cathode current, mA	391	380

(b) High mode

Parameter	Analytical design value	Experimental value for TWT
Cathode voltage, kV	9.9	9.75
Cathode current, mA	488	475

TABLE III.—INPUT AND OUTPUT DISK ENERGIES OF REFOCUSING SYSTEM FOR SATURATED OPERATION

(a) High mode

Trajectory	Disk energy, E, keV	
	Input	Output
1	6.8	5.9
2	10.4	10.6
3	11.4	10.1
4	8.2	6.3
5	7.6	5.6
6	9.2	9.6
7	6.9	5.5
8	6.9	6.1
9	8.6	11.0
10	6.7	5.7
11	7.4	7.9
12	7.4	8.7
13	4.6	5.0
14	5.7	5.9
15	4.6	6.2
16	5.3	5.9
17	5.1	6.9
18	6.0	6.1
19	5.9	6.1
20	8.9	9.3
21	11.2	8.9
22	5.6	7.9
23	7.8	9.3
24	6.9	9.8
25	6.2	5.9
26	6.2	5.4
27	4.8	4.3
28	11.0	9.3
29	6.9	5.5
30	7.7	10.3
31	10.0	9.5
32	10.8	8.9
$\overline{E}$	7.47	7.47
$\sigma_n(E)$	1.98	1.93

(b) Low mode

Trajectory	Disk energy, E, keV	
	Input	Output
1	7.0	7.5
2	9.8	10.0
3	11.2	9.7
4	8.2	6.9
5	7.2	9.3
6	10.8	8.7
7	10.6	7.8
8	7.6	6.2
9	8.8	9.5
10	5.9	6.8
11	9.7	6.7
12	8.4	9.0
13	7.2	5.8
14	9.1	8.2
15	7.2	7.0
16	6.9	5.3
17	8.4	9.3
18	5.4	6.2
19	8.3	9.9
20	7.4	8.1
21	5.1	6.2
22	7.2	8.7
23	8.3	9.9
24	7.9	8.2
25	4.7	5.1
26	9.0	10.1
27	10.1	10.2
28	9.7	9.6
29	6.6	8.3
30	10.6	9.8
31	4.9	5.3
32	8.8	9.7
$\overline{E}$	8.07	8.08
$\sigma_n(E)$	1.73	1.61

TABLE IV.—INPUT AND OUTPUT ANGLES OF DISK EDGE OF REFOCUSING SYSTEM FOR SATURATED OPERATION

(a) High mode

Trajectory	Disk-edge angle, θ deg	
	Input	Output
1	0.6	−4.6
2	−2.1	−1.6
3	−.2	−.8
4	−1.8	−3.9
5	−2.5	−4.0
6	−.05	−4.2
7	−2.7	5.1
8	−2.5	4.0
9	−2.2	−.7
10	−3.7	−1.5
11	−3.2	−6.8
12	−2.8	−5.1
13	−2.9	−8.2
14	−2.9	1.0
15	.2	1.3
16	−3.6	3.4
17	3.1	4.6
18	8.3	4.6
19	7.3	1.0
20	4.4	.3
21	3.9	−.5
22	3.8	−.02
23	5.1	−6.1
24	−.4	1.0
25	6.3	.5
26	3.5	−4.9
27	.9	−7.2
28	2.0	2.2
29	2.6	5.5
30	1.8	−3.7
31	.1	1.1
32	−2.4	2.0
$\overline{\theta}$	.6	−.8
$\sigma_n(\theta)$	3.4	3.8
Number of negative angles	16	17

(b) Low mode

Trajectory	Disk-edge angle, θ deg	
	Input	Output
1	2.1	−1.0
2	.8	.1
3	.8	3.0
4	−3.1	−4.8
5	2.4	−3.9
6	−1.3	2.0
7	.2	1.3
8	−1.8	−3.3
9	−.7	−2.6
10	−1.8	−6.3
11	−2.2	−4.5
12	−2.0	−.5
13	2.4	4.9
14	−1.4	−3.9
15	.03	−4.0
16	.4	3.9
17	2.5	−.9
18	−2.3	−.03
19	−1.6	−.7
20	−2.9	−.01
21	−3.2	−3.5
22	−5.3	−4.7
23	1.6	−5.9
24	−1.5	−3.5
25	−.4	−4.9
26	3.7	−2.7
27	2.8	2.6
28	2.8	.2
29	4.6	−.6
30	2.9	4.4
31	2.6	−3.8
32	2.2	3.8
$\overline{\theta}$	.11	−1.2
$\sigma_n(\theta)$	2.4	3.2
Number of negative angles	15	22

TABLE V.—INPUT AND OUTPUT RADII OF DISK EDGE OF REFOCUSING
SYSTEM FOR SATURATED OPERATION

(a) High mode (b) Low mode

Trajectory	Disk-edge radius, r, m		Trajectory	Disk-edge radius, r, m	
	Input	Output		Input	Output
1	7.8×10^{-4}	8.1×10^{-4}	1	6.5×10^{-4}	7.5×10^{-4}
2	7.6	11.0	2	9.4	7.3
3	5.6	11.4	3	8.4	7.2
4	8.9	7.9	4	6.8	8.3
5	9.4	6.5	5	4.8	5.6
6	6.8	9.0	6	6.7	9.3
7	8.6	4.7	7	7.6	9.1
8	8.2	3.3	8	6.4	4.2
9	9.2	8.1	9	7.0	9.7
10	6.6	3.1	10	2.1	7.8
11	3.6	10.9	11	5.1	10.0
12	4.5	12.3	12	7.4	9.3
13	6.4	8.5	13	7.1	3.0
14	9.6	7.6	14	5.9	11.1
15	4.0	8.3	15	6.2	9.1
16	5.5	9.0	16	6.4	3.1
17	3.2	5.0	17	7.2	5.5
18	6.0	3.4	18	5.7	8.3
19	6.3	4.3	19	8.2	6.8
20	3.9	1.6	20	5.8	12.7
21	7.6	6.0	21	2.9	8.9
22	5.0	5.6	22	4.0	13.9
23	4.4	4.0	23	3.5	5.0
24	9.4	7.4	24	3.4	10.4
25	7.3	4.7	25	2.2	2.8
26	6.3	4.4	26	3.9	2.9
27	7.0	3.8	27	7.3	2.7
28	7.3	4.3	28	4.5	3.0
29	7.0	2.4	29	6.7	5.2
30	5.3	4.7	30	8.2	5.7
31	6.1	4.7	31	7.5	15.4
32	8.5	11.0	32	7.6	3.1
$\bar{r}$	6.7	6.5	$\bar{r}$	6.0	7.3

TABLE VI.—ANALYTICAL AND EXPERIMENTAL PERFORMANCES
OF TWT 001 AND 2.4-cm-DIAMETER, FOUR-STAGE, DEPRESSED
COLLECTOR, WITH TWT OPERATING AT SATURATION AT
8.4 GHz IN LOW MODE AND WITH ANALYTICAL
COLLECTOR VOLTAGES

[Computed trajectories shown in fig. 5. Voltages, currents, and powers given as percentages of V_0, I_0, and $V_0 I_0$, respectively, where V_0 is cathode potential with respect to ground and I_0 is beam current.]

(a) MDC performance

Collecting element	Voltage	Analytical		Experimental	
		Current	Recovered power	Current	Recovered power
TWT body (interception)	0	0	0	5.5	0
TWT body (backstreaming)	0	5.0	0		0
Collector electrode:					
1	54.5	31.3	17.0	49.4	26.9
2	74.7	25.6	19.2	13.0	9.7
3	89.9	35.6	32.0	31.3	28.1
4	100	2.5	2.5	.7	.7
Collector efficiency, η_{col}, percent		83.4		82.3	
Overall efficiency, η_{ov}, percent		46.1		48.5	

(b) Final power distribution

Components of power	Analytical	Experimental
RF output power	13.5	16.8
Total RF power losses (including circuit and sever losses)	1.7	(a)
Beam interception losses	0	(a)
Backstreaming to TWT body	2.7	(a)
MDC dissipation	11.3	(a)
Recovered power	70.7	65.4

[a]Not measured.

14

TABLE VII.—ANALYTICAL AND EXPERIMENTAL PERFORMANCES OF TWT 001 AND
2.4-cm-DIAMETER, FOUR-STAGE, DEPRESSED COLLECTOR, WITH TWT
OPERATING AT SATURATION AT 8.4 GHz IN HIGH MODE AND
WITH ANALYTICAL COLLECTOR VOLTAGES

[Computed trajectories shown in fig. 6. Voltages, currents, and powers given as percentages of V_0, I_0, and $V_0 I_0$, respectively, where V_0 is cathode potential with respect to ground and I_0 is beam current.]

(a) MDC performance

Collecting element	Voltage	Analytical		Experimental			
				$I_0 = 0.417$ A		$I_0 = 0.475$ A	
		Current	Recovered power	Current	Recovered power	Current	Recovered power
TWT body (interception)	0	0	0	} 6.7	0	} 12.1	0
TWT body (backstreaming)	0	6.3	0		0		0
Collector electrode:							
1	54.5	51.9	28.3	49.5	27.0	44.5	24.3
2	74.7	8.1	6.1	12.6	9.4	14.4	10.8
3	89.9	31.3	28.1	30.3	27.2	27.4	24.6
4	100	2.5	2.5	.8	.8	1.6	1.6
Collector efficiency, η_{col}, percent		81.7		81.4		78.0	
Overall efficiency, η_{ov}, percent		50.4		48.3		41.9	

(b) Final power distribution

Components of power	Analytical	Experimental	
		$I_0 = 0.417$ A	$I_0 = 0.475$ A
RF output power	17.6	17.1	16.2
Total RF power losses (including circuit and sever losses)	2.8	(a)	(a)
Beam interception losses	0	(a)	(a)
Backstreaming to TWT body	3.2	(a)	(a)
MDC dissipation	11.4	(a)	(a)
Recovered power	65.0	64.4	61.3

[a]Not measured.

TABLE VIII.—ANALYTICAL AND EXPERIMENTAL PERFORMANCES
OF TWT 001 AND 2.4-cm-DIAMETER, FOUR-STAGE, DEPRESSED
COLLECTOR, WITH TWT OPERATING AT SATURATION AT
8.4 GHz IN LOW MODE AND WITH EXPERIMENTALLY
OPTIMIZED COLLECTOR VOLTAGES

[Computed trajectories shown in fig. 7. Voltages, currents, and powers given as percentages of V_0, I_0, and $V_0 I_0$, respectively, where V_0 is cathode potential with respect to ground and I_0 is beam current.]

(a) MDC performance

Collecting element	Voltage	Analytical		Experimental	
		Current	Recovered power	Current	Recovered power
TWT body (interception)	0	0	0	} 3.9	0
TWT body (backstreaming)	0	5.0	0		0
Collector electrode:					
1	54.5	23.7	13.0	36.8	20.1
2	65.6	25.0	16.4	22.5	14.8
3	85.1	45.0	38.3	36.4	31.0
4	100	1.3	1.3	.3	.3
Collector efficiency, η_{col}, percent		81.3		83.2	
Overall efficiency, η_{ov}, percent		43.4		49.7	

(b) Final power distribution

Components of power	Analytical	Experimental
RF output power	13.5	16.8
Total RF power losses (including circuit and sever losses)	1.7	(a)
Beam interception losses	0	(a)
Backstreaming to TWT body	2.7	(a)
MDC dissipation	13.1	(a)
Recovered power	68.9	66.1

[a]Not measured.

TABLE IX.—ANALYTICAL AND EXPERIMENTAL PERFORMANCES OF TWT 001 AND
2.4-cm-DIAMETER, FOUR-STAGE, DEPRESSED COLLECTOR, WITH TWT
OPERATING AT SATURATION AT 8.4 GHz IN HIGH MODE AND
WITH EXPERIMENTALLY OPTIMIZED COLLECTOR VOLTAGES

[Computed trajectories shown in fig. 8. Voltages, currents, and powers given as percentages of V_0, I_0, and $V_0 I_0$, respectively, where V_0 is cathode potential with respect to ground and I_0 is beam current.]

(a) MDC performance

Collecting element	Voltage	Analytical		Experimental			
				$I_0 = 0.417$ A		$I_0 = 0.475$ A	
		Current	Recovered power	Current	Recovered power	Current	Recovered power
TWT body (interception)	0	0	0	} 5.0	0	} 11.1	0
TWT body (backstreaming)	0	6.3	0		0		0
Collector electrode:							
1	54.5	45.6	24.9	38.6	21.0	36.8	20.0
2	65.6	11.3	7.4	19.8	13.0	16.2	10.6
3	85.1	34.4	29.3	36.2	30.9	35.1	29.8
4	100	2.5	2.5	.3	.3	1.1	1.1
Collector efficiency, η_{col}, percent		80.5		82.3		78.4	
Overall efficiency, η_{ov}, percent		49.1		49.3		42.6	

(b) Final power distribution

Components of power	Analytical	Experimental	
		$I_0 = 0.417$ A	$I_0 = 0.475$ A
RF output power	17.6	17.2	16.4
Total RF power losses (including circuit and sever losses)	2.8	(a)	(a)
Beam interception losses	0	(a)	(a)
Backstreaming to TWT body	3.2	(a)	(a)
MDC dissipation	12.3	(a)	(a)
Recovered power	64.0	65.1	61.6

[a]Not measured.

17

TABLE X.—SUMMARY OF ANALYTICAL AND EXPERIMENTAL RESULTS FOR TWT 001 AND FOUR-STAGE MDC, WITH TWT OPERATING AT SATURATION AT 8.4 GHz

(a) Low mode

MDC operating conditions	RF efficiency, η_{RF}, percent		Overall efficiency, η_{ov}, percent		Collector efficiency, η_{col}, percent	
	Analytical	Experimental	Analytical	Experimental	Analytical	Experimental
Design voltages	13.5	16.8	46.1	48.5	83.4	82.3
Experimentally optimized voltages	13.5	16.8	43.4	49.7	81.3	83.2

(b) High mode

MDC operating conditions	RF efficiency, η_{RF}, percent			Overall efficiency, η_{ov}, percent			Collector efficiency, η_{col}, percent		
	Analytical[a]	Experimental		Analytical[a]	Experimental		Analytical[a]	Experimental	
		$I_0 = 0.417$ A	$I_0 = 0.475$ A		$I_0 = 0.417$ A	$I_0 = 0.475$ A		$I_0 = 0.417$ A	$I_0 = 0.475$ A
Design voltages	17.6	17.1	16.2	50.4	48.3	41.9	81.7	81.4	78.0
Experimentally optimized voltages	17.6	17.2	16.4	49.1	49.3	42.6	80.5	82.4	78.4

[a]Beam current I_0, 0.488 A.

TABLE XI.—COMPUTED TWT AND FOUR-STAGE COLLECTOR EFFICIENCIES WITH AND WITHOUT SECONDARY-ELECTRON-EMISSION LOSSES, WITH TWT OPERATING AT SATURATION AT 8.4 GHz IN LOW MODE

(a) Overall TWT efficiency, η_{ov}

MDC operating condition	Efficiency, percent	
	Without secondary-electron-emission losses	With secondary-electron-emission losses
Design voltages	50.6	46.1
Experimentally optimized voltages	47.1	43.4

(b) Collector efficiency, η_{col}

MDC operating condition	Efficiency, percent	
	Without secondary-electron-emission losses	With secondary-electron-emission losses
Design voltages	86.5	83.4
Experimentally optimized voltages	84.2	81.3

TABLE XII.—COMPUTED TWT AND FOUR-STAGE COLLECTOR EFFICIENCIES WITH AND WITHOUT SECONDARY-ELECTRON-EMISSION LOSSES, WITH TWT OPERATING AT SATURATION AT 8.4 GHz IN HIGH MODE

(a) Overall TWT efficiency, η_{ov}

MDC operating condition	Efficiency, percent	
	Without secondary-electron-emission losses	With secondary-electron-emission losses
Design voltages	52.3	50.4
Experimentally optimized voltages	51.2	49.1

(b) Collector efficiency, η_{col}

MDC operating condition	Efficiency, percent	
	Without secondary-electron-emission losses	With secondary-electron-emission losses
Design voltages	83.4	81.7
Experimentally optimized voltages	82.4	80.5

TABLE XIII.—ANALYTICAL AND EXPERIMENTAL PERFORMANCES
OF TWT 001 AND 2.4-cm-DIAMETER, THREE-STAGE, DEPRESSED
COLLECTOR, WITH TWT OPERATING AT SATURATION AT
8.4 GHz IN LOW MODE AND WITH EXPERIMENTALLY
OPTIMIZED COLLECTOR VOLTAGES

[Computed trajectories shown in fig. 9. Voltages, currents, and powers given as percentages of V_0, I_0, and $V_0 I_0$, respectively, where V_0 is cathode potential with respect to ground and I_0 is beam current.]

(a) MDC performance

Collecting element	Voltage	Analytical		Experimental	
		Current	Recovered power	Current	Recovered power
TWT body (interception)	0	0	0	} 3.4	0
TWT body (backstreaming)	0	3.1	0		0
Collector electrode:					
1	53.8	18.7	10.1	13.6	7.3
2	53.8	31.3	16.8	42.2	22.7
3	83.6	45.6	38.1	40.7	34.0
4	100	1.3	1.3	.2	.2
Collector efficiency, η_{col}, percent		78.2		80.5	
Overall efficiency, η_{ov}, percent		40.0		46.1	

(b) Final power distribution

Components of power	Analytical	Experimental
RF output power	13.5	16.5
Total RF power losses (including circuit and sever losses)	1.7	(a)
Beam interception losses	0	(a)
Backstreaming to TWT body	1.7	(a)
MDC dissipation	16.8	(a)
Recovered power	66.3	64.2

[a]Not measured.

TABLE XIV.—ANALYTICAL AND EXPERIMENTAL PERFORMANCES OF TWT 001 AND
2.4-cm-DIAMETER, THREE-STAGE, DEPRESSED COLLECTOR, WITH TWT
OPERATING AT SATURATION AT 8.4 GHz IN HIGH MODE AND WITH
EXPERIMENTALLY OPTIMIZED COLLECTOR VOLTAGES

[Computed trajectories shown in fig. 10. Voltages, currents, and powers given as percentages of V_0, I_0, and $V_0 I_0$, respectively, where V_0 is cathode potential with respect to ground and I_0 is beam current.]

(a) MDC performance

Collecting element	Voltage	Analytical		Experimental			
				$I_0 = 0.417$ A		$I_0 = 0.475$ A	
		Current	Recovered power	Current	Recovered power	Current	Recovered power
TWT body (interception)	0	0	0	} 4.6	0	} 10.4	0
TWT body (backstreaming)	0	9.4	0		0		0
Collector electrode:							
1	53.8	18.8	10.1	12.7	6.8	12.0	6.5
2	53.8	35.0	18.8	43.9	23.6	39.3	21.2
3	83.6	34.4	28.7	38.7	32.3	37.5	31.3
4	100	2.5	2.5	.3	.3	.9	.9
Collector efficiency, η_{col}, percent		75.7		79.8		76.2	
Overall efficiency, η_{ov}, percent		44.3		46.5		40.8	

(b) Final power distribution

Components of power	Analytical	Experimental	
		$I_0 = 0.417$ A	$I_0 = 0.475$ A
RF output power	17.6	17.1	16.4
Total RF power losses (including circuit and sever losses)	2.8	(a)	(a)
Beam interception losses	0	(a)	(a)
Backstreaming to TWT body	5.8	(a)	(a)
MDC dissipation	13.5	(a)	(a)
Recovered power	60.2	63.1	59.9

[a]Not measured.

20

TABLE XV.—ANALYTICAL AND EXPERIMENTAL PERFORMANCES
OF TWT 001 AND 2.4-cm-DIAMETER, THREE-STAGE, DEPRESSED
COLLECTOR, WITH TWT OPERATING AT SATURATION AT
8.4 GHz IN LOW MODE AND WITH REDUCED
COLLECTOR VOLTAGE

[Computed trajectories shown in fig. 11. Voltages, currents, and powers given as percentages of V_0, I_0, and $V_0 I_0$, respectively, where V_0 is cathode potential with respect to ground and I_0 is beam current.]

(a) MDC performance

Collecting element	Voltage	Analytical		Experimental	
		Current	Recovered power	Current	Recovered power
TWT body (interception)	0	0	0	3.0	0
TWT body (backstreaming)	0	3.1	0		0
Collector electrode:					
1	53.8	13.7	7.4	10.5	5.7
2	53.8	26.3	14.1	45.2	24.3
3	81.1	55.6	45.1	41.1	33.3
4	100	1.3	1.3	.3	.3
Collector efficiency, η_{col}, percent		80.1		79.8	
Overall efficiency, η_{ov}, percent		42.0		45.4	

(b) Final power distribution

Components of power	Analytical	Experimental
RF output power	13.5	16.6
Total RF power losses (including circuit and sever losses)	1.7	(a)
Beam interception losses	0	(a)
Backstreaming to TWT body	1.7	(a)
MDC dissipation	15.2	(a)
Recovered power	67.9	63.6

[a]Not measured.

TABLE XVI.—ANALYTICAL AND EXPERIMENTAL PERFORMANCES OF TWT 001 AND 2.4-cm-DIAMETER, THREE-STAGE, DEPRESSED COLLECTOR, WITH TWT OPERATING AT SATURATION AT 8.4 GHz IN HIGH MODE AND WITH REDUCED COLLECTOR VOLTAGE

[Computed trajectories shown in fig. 12. Voltages, currents, and powers given as percentages of V_0, I_0, and $V_0 I_0$, respectively, where V_0 is cathode potential with respect to ground and I_0 is beam current.]

(a) MDC performance

Collecting element	Voltage	Analytical		Experimental			
				$I_0 = 0.417$ A		$I_0 = 0.475$ A	
		Current	Recovered power	Current	Recovered power	Current	Recovered power
TWT body (interception)	0	0	0	} 4.0	0	} 9.4	0
TWT body (backstreaming)	0	6.3	0		0		0
Collector electrode:							
1	53.8	17.5	9.4	10.7	5.8	10.2	5.5
2	53.8	36.3	19.5	44.1	23.8	40.0	21.5
3	81.1	37.5	30.4	41.0	33.2	39.7	32.2
4	100	2.5	2.5	.3	.3	.7	.7
Collector efficiency, η_{col}, percent		77.8		79.7		76.5	
Overall efficiency, η_{ov}, percent		46.2		46.4		41.3	

(b) Final power distribution

Components of power	Analytical	Experimental	
		$I_0 = 0.417$ A	$I_0 = 0.475$ A
RF output power	17.6	17.2	16.5
Total RF power losses (including circuit and sever losses)	2.8	(a)	(a)
Beam interception losses	0	(a)	(a)
Backstreaming to TWT body	3.2	(a)	(a)
MDC dissipation	14.5	(a)	(a)
Recovered power	61.8	63.0	59.9

[a]Not measured.

TABLE XVII.—SUMMARY OF ANALYTICAL AND EXPERIMENTAL RESULTS FOR TWT 001 AND THREE-STAGE MDC, WITH TWT OPERATING AT SATURATION AT 8.4 GHz

(a) Low mode

MDC operating conditions	RF efficiency, η_{RF}, percent		Overall efficiency, η_{ov}, percent		Collector efficiency, η_{col}, percent	
	Analytical	Experimental	Analytical	Experimental	Analytical	Experimental
Experimentally optimized voltages	13.5	16.7	40.0	46.1	78.2	80.5
Reduced voltage	13.5	16.6	42.0	45.5	80.1	79.8

(b) High mode

MDC operating conditions	RF efficiency, η_{RF}, percent			Overall efficiency, η_{ov}, percent			Collector efficiency, η_{col}, percent		
	Analytical[a]	Experimental		Analytical[a]	Experimental		Analytical[a]	Experimental	
		$I_0 = 0.417$ A	$I_0 = 0.475$ A		$I_0 = 0.417$ A	$I_0 = 0.475$ A		$I_0 = 0.417$ A	$I_0 = 0.475$ A
Experimentally optimized voltages	17.6	17.1	16.4	44.3	46.5	40.8	75.7	79.8	76.2
Reduced voltage	17.6	17.2	16.5	46.2	46.4	41.3	77.8	79.7	76.5

[a]Beam current I_0, 0.488 A.

TABLE XVIII.—COMPUTED TWT AND THREE-STAGE COLLECTOR EFFICIENCIES WITH AND WITHOUT SECONDARY-ELECTRON-EMISSION LOSSES, WITH TWT OPERATING AT SATURATION AT 8.4 GHz IN LOW MODE

(a) Overall TWT efficiency, η_{ov}

MDC operating condition	Efficiency, percent	
	Without secondary-electron-emission losses	With secondary-electron-emission losses
Experimentally optimized voltages	44.0	40.0
Reduced voltage	44.6	42.0

(b) Collector efficiency, η_{col}

MDC operating condition	Efficiency, percent	
	Without secondary-electron-emission losses	With secondary-electron-emission losses
Experimentally optimized voltages	81.8	78.2
Reduced voltage	82.3	80.1

TABLE XIX.—COMPUTED TWT AND THREE-STAGE COLLECTOR EFFICIENCIES WITH AND WITHOUT SECONDARY-ELECTRON-EMISSION LOSSES, WITH TWT OPERATING AT SATURATION AT 8.4 GHz IN HIGH MODE

(a) Overall TWT efficiency, η_{ov}

MDC operating condition	Efficiency, percent	
	Without secondary-electron-emission losses	With secondary-electron-emission losses
Experimentally optimized voltages	46.3	44.3
Reduced voltage	48.4	46.2

(b) Collector efficiency, η_{col}

MDC operating condition	Efficiency, percent	
	Without secondary-electron-emission losses	With secondary-electron-emission losses
Experimentally optimized voltages	77.9	75.7
Reduced voltage	80.0	77.8

NASA
National Aeronautics and Space Administration

Report Documentation Page

1. Report No. NASA TP-2752	2. Government Accession No.	3. Recipient's Catalog No.

4. Title and Subtitle

Analytical and Experimental Performance of a Dual-Mode Traveling-Wave Tube and Multistage Depressed Collector

5. Report Date

August 1987

6. Performing Organization Code

506-44-21

7. Author(s)

Peter Ramins, Dale A. Force, and Henry G. Kosmahl

8. Performing Organization Report No.

E-3470

10. Work Unit No.

9. Performing Organization Name and Address

National Aeronautics and Space Administration
Lewis Research Center
Cleveland, Ohio 44135

11. Contract or Grant No.

13. Type of Report and Period Covered

Technical Paper

12. Sponsoring Agency Name and Address

National Aeronautics and Space Administration
Washington, D.C. 20546

14. Sponsoring Agency Code

15. Supplementary Notes

Henry G. Kosmahl, retired from NASA Lewis Research Center; presently with Analex Corporation, Cleveland, Ohio 44135.

16. Abstract

A computational procedure for the design of traveling-wave-tube (TWT)/refocuser/multistage depressed collector (MDC) systems was used to design a short, permanent-magnet refocusing system and a highly efficient MDC for a medium-power, dual-mode, 4.8- to 9.6-GHz TWT. The computations were carried out with advanced, multi-dimensional computer programs which model the electron beam and follow the trajectories of representative charges from the radiofrequency (RF) input of the TWT, through the slow-wave structure and refocusing section, to their points of impact in the depressed collector. Secondary emission losses in the MDC were treated semi-quantitatively by injecting representative secondary-electron-emission current into the MDC analysis at the point of impact of each primary beam. A comparison of computed and measured TWT and MDC performance showed very good agreement. The electrodes of the MDC were fabricated from a particular form of isotropic graphite that was selected for its low secondary electron yield, ease of machinability, and vacuum properties.

17. Key Words (Suggested by Author(s))	18. Distribution Statement
Computer-aided design Traveling-wave tube Multistage depressed collector Spent-beam refocusing	Unclassified—unlimited STAR Category 33

19. Security Classif. (of this report)	20. Security Classif. (of this page)	21. No of pages	22. Price*
Unclassified	Unclassified	26	A03